Observations of Ionospheric ELF and VLF Wave Generation by Excitation of the Thermal Cubic Nonlinearity

R. C. Moore,[1,*] S. Fujimaru,[1] D. A. Kotovsky,[1] and M. Gołkowski[2]

[1]*Department of Electrical and Computer Engineering, University of Florida, Gainesville, Florida 32611, USA*

[2]*Department of Electrical Engineering, University of Colorado Denver, Denver, Colorado 80202, USA*

(Received 19 June 2013; published 6 December 2013)

Extremely-low-frequency (ELF, 3–3000 Hz) and very-low-frequency (VLF, 3–30 kHz) waves generated by the excitation of the thermal cubic nonlinearity are observed for the first time at the High-Frequency Active Auroral Research Program high-frequency transmitter in Gakona, Alaska. The observed ELF and VLF field amplitudes are the strongest generated by any high frequency (HF, 3–30 MHz) heating facility using this mechanism to date. This manner of ELF and VLF generation is independent of naturally forming currents, such as the auroral electrojet current system. Time-of-arrival analysis applied to experimental observations shows that the thermal cubic ELF and VLF source region is located within the collisional *D*-region ionosphere. Observations are compared with the predictions of a theoretical HF heating model using perturbation theory. For the experiments performed, two *X*-mode HF waves were transmitted at frequencies ω_1 and ω_2, with $|\omega_2 - 2\omega_1|$ being in the ELF and VLF frequency range. In contrast with previous work, we determine that the ELF and VLF source is dominantly produced by the interaction between collision frequency oscillations at frequency $\omega_2 - \omega_1$ and the polarization current density associated with the lower frequency HF wave at frequency ω_1. This specific interaction has been neglected in past cubic thermal nonlinearity work, and it plays a major role in the generation of ELF and VLF waves.

DOI: 10.1103/PhysRevLett.111.235007 PACS numbers: 94.20.Tt, 52.25.Os, 52.35.Mw, 52.50.Qt

Introduction.—Extremely-low-frequency (ELF, 3–3000 Hz) and very-low-frequency (VLF, 3–30 kHz) electromagnetic waves have been regularly produced by modulated high frequency (HF, 3–30 MHz) heating of the *D*-region ionosphere ($\sim$ 60–100 km altitude) in the presence of naturally occurring electric currents, such as the auroral electrojet [1–9]. Magnitudes of ELF and VLF waves generated in this manner are highly dependent upon the geomagnetic conditions that drive the strength of the electrojet, which varies significantly with time [5,10–13]. In an effort to improve the reliability of ELF and VLF wave generation by ionospheric heating, recent experiments at the High-frequency Active Auroral Research Program (HAARP) facility in Gakona, Alaska, have focused on developing wave generation methods that are independent of the strength of the electrojet currents [14,15]. This Letter investigates the excitation of the thermal cubic nonlinearity [16–19] as another electrojet-independent method to generate ELF and VLF waves.

The viability of the ''cubic'' wave generation mechanism has been demonstrated previously in Russia using HF transmissions [19] and in Norway using VLF transmissions [18]. ELF and VLF amplitudes on the order of 1–10 fT were generated using HF signals [19], whereas VLF signal amplitudes on the order of 10–20 fT were generated using VLF signals [18], despite the much lower power of the transmitters involved.

Excitation of the cubic thermal nonlinearity involves interactions between the electric fields and the polarization current densities associated with two high-power radio waves with frequencies ω_1 and ω_2, with $\omega_2 \approx 2\omega_1$. Previous work suggests that the lower frequency wave induces a collision frequency oscillation at twice its frequency and that this collision frequency oscillation mixes with the polarization current density of the higher frequency wave to produce an ELF and VLF source current density at frequency $|\omega_2 - 2\omega_1|$ [17,19]. In this Letter, we describe the first numerical modeling of the cubic thermal nonlinearity mechanism and demonstrate that, in contrast to previous work, the ELF and VLF source is dominantly produced by the mixing of collision frequency components at the difference frequency $(\omega_2 - \omega_1)$ with the lower frequency wave (ω_1).

Experiment description.—On May 3 and 9, 2012, the 3.6 MW HAARP HF transmitter (62.39 °N, 145.2 °W) performed dual-beam cw HF heating experiments. The 12×15 element HAARP array was split evenly in either the north-south or the east-west direction to create two subarrays. For the north-south split, the north array broadcasted a $\sim$2.75 MHz (ω_1) *X*-mode cw signal with 77 dBW effective radiated power (ERP) while the south array broadcasted a $\sim$5.5 MHz (ω_2) *X*-mode cw signal with 86 dBW ERP. For the east-west split, the west array broadcasted the $\sim$2.75 MHz signal, while the east array broadcasted the $\sim$5.5 MHz signal. In both cases, both HF beams were directed toward magnetic zenith (14° zenith angle, 202° east of north).

To allow time-of-arrival (TOA) analysis [20] to be applied to the received ELF and VLF waveforms, the frequencies of the two cw signals varied linearly with time, creating FM-cw chirps. Four combinations of 30 second duration linear FM-cw chirps were employed, as listed in Table I. The first two combinations were intended to generate ELF and VLF frequency-time ramps from 1.000–5.080 kHz, while the second two combinations were intended to generate VLF frequency-time ramps from 16.000–20.080 kHz.

HF observations were performed at Oasis (OA, 62.35 °N, 145.1 °W, 3.3 km from HAARP) to provide an accurate measurement of the HAARP transmission. The HF receiving system consists of two orthogonal 27-meter folded dipoles located ~4 meters above the ground. The receiver is sensitive to electric fields between 1.0 and 10.0 MHz, and data acquisition is performed continuously at 25 MHz with 14-bit resolution. Accurate timing is provided by GPS.

ELF and VLF (300 Hz–45 kHz) observations were performed at Oasis (location listed above) and at Paradise (PD, 62.52 °N, 143.2 °W, 98 km from HAARP). Each receiver system consists of two orthogonal magnetic loop antennas oriented to detect the radial and azimuthal components of the magnetic field at ground level, a preamplifier, a line receiver, and a digitizing computer. Accurate timing is provided by GPS.

In postprocessing, ELF and VLF chirps detected at the receivers are mixed to the baseband and filtered to reduce noise. The resulting signals are then mixed back to the original ELF and VLF frequency range. Time-of-arrival analysis is performed by calculating the positive-frequency impulse response of the system. This response is calculated by dividing the Fourier transform of the reduced-noise ELF and VLF signal by the Fourier transform of the expected ELF and VLF radiation, and converting to the time domain. The expected ELF and VLF radiation is calculated as $\omega_2 - 2\omega_1$, with ω_1 and ω_2 experimentally measured by the HF receiving system at Oasis.

During the experiments, the background geomagnetic and ionospheric conditions were fairly typical for HAARP's subauroral location. On May 3, 2012, the HAARP magnetometer exhibited a variation between ~50–100 nT, while the HAARP 30 MHz riometer exhibited ~0.1–0.2 dB absorption. On May 9, 2012, the HAARP magnetometer was quiet at ~25 nT, while the HAARP riometer exhibited ~0.4–0.6 dB absorption. The HAARP digisonde did not register any valid *X*-mode ionospheric echoes during either transmission period.

TABLE I. Transmission frequency combinations.

	Beam 1		Beam 2	
Combination	Start freq. (MHz)	Slope (Hz/sec)	Start freq. (MHz)	Slope (Hz/sec)
1	2.750 250	+34	5.499 500	−68
2	2.749 750	−34	5.500 500	+68
3	2.754 000	+34	5.492 000	−68
4	2.746 000	−34	5.508 000	+68

Experimental observations.—On May 9, 2012, VLF signals in the 16–20 kHz range were visually detectable in spectrograms at both Oasis and Paradise. Figure 1 shows VLF spectrograms of the detected signals together with the ambient noise environment at both locations. The signal is clearly detected at both sites as a frequency-time chirp with its frequency varying linearly between 16 and 20 kHz over the course of 30 seconds. We point out that the color scales on the two plots are slightly different to best highlight the detected VLF chirp at both sites. ELF and VLF signals in the 1–5 kHz range were not detectable at this time.

Applying TOA analysis to the May 9, 2012 VLF observations shown in Fig. 1 results in the impulse responses shown in Fig. 2. Due to the presence of interference at 16.4 kHz, we limited the frequency range of the VLF signal to 16.5–20.0 kHz. The peak amplitude at Oasis, which is only 3 km from HAARP, is ~13 dB stronger than the peak amplitude detected at Paradise, which is 98 km from HAARP. The peak amplitudes occur at ~0.45 msec at Oasis and at ~0.6 msec at Paradise. Assuming the VLF source is located directly above the HF transmitter, these propagation delays correspond to virtual source altitudes of 68 and 63 km, respectively.

For the May 9 case, the relatively high (> 10 dB) signal-to-noise ratio (SNR) allows us to determine whether additional VLF sources exist at higher ionospheric altitudes. As can be seen in Fig. 2, no additional signals are detected

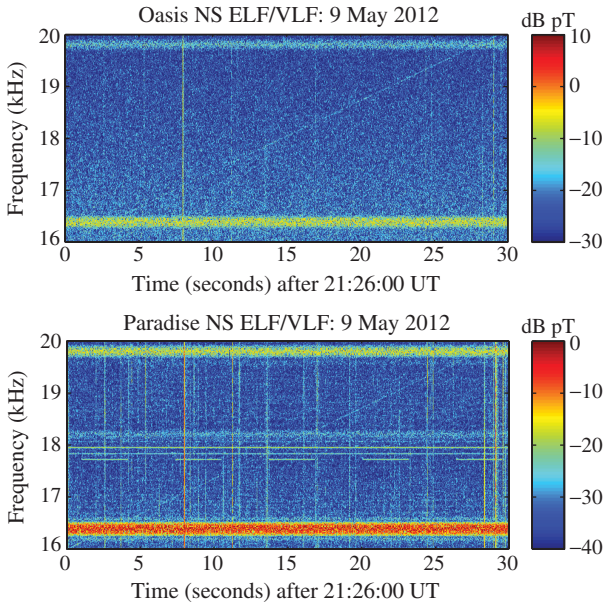

FIG. 1 (color). Spectrogram format ELF and VLF observations performed at Oasis and Paradise showing the detection of the 16–20 kHz ramp at both locations.

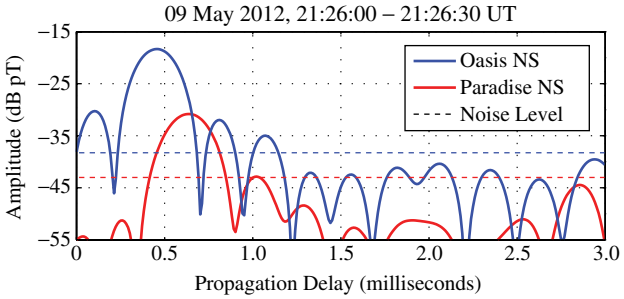

FIG. 2 (color online). TOA analysis of simultaneous ELF and VLF observations performed at Oasis and Paradise for the 16.5–20.0 kHz ramp.

above the noise floor beyond a 1.25 msec propagation delay, clearly pointing to a source at *D*-region altitudes.

Figure 3 shows the TOA analysis applied to ELF and VLF observations performed on May 3, 2012. On this day, both the 1–5 kHz and the 16–20 kHz ELF and VLF chirps were detected with >6 dB signal-to-noise ratio (SNR) within minutes of each other. In this case, signals were not visually detectable in spectrograms and detection required integrating over the majority of the 30 second duration. We limit the frequency range of the VLF signal to 16.5–20.0 kHz due to the presence of the 16.4 kHz interference, and to produce comparable results for the lower frequency range, we limit its range to 1.5–5.0 kHz. For both frequency ranges, the peak amplitude occurs with a propagation delay between 0.40 and 0.55 msec, corresponding to a virtual source altitude between 60 and 83 km. The amplitude of the 1.5–5.0 kHz chirp is ~15 dB lower than that of the 16.5–20.0 kHz chirp, an observation that is opposite to the frequency dependence observed at the Sura heating facility [19]. Other pulses that occur in both responses after ~1.5 msec are within 3 dB of the respective noise floors, and they cannot be distinguished from noise elements.

On both days, and for both frequency ranges, ELF and VLF signals were observed with >6 dB SNR only when the HAARP array was split in the north-south direction and

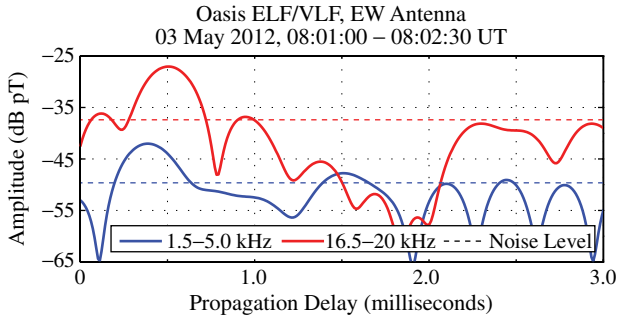

FIG. 3 (color online). ELF and VLF observations performed at Oasis showing the detection of both the 1.5–5.0 kHz and the 16.5–20.0 kHz ramps using TOA analysis.

only for combinations 2 and 4 listed in Table I. This effect most likely results from the HF interference pattern produced by the physical separation of the north and south HAARP subarrays. Similar effects have been observed during "beat-wave" ELF and VLF wave generation experiments: the lateral separation of the phase centers of the two transmitting subarrays produces a HF phasing pattern at ionospheric altitudes that in turn results in a highly directional ELF and VLF radiation pattern [21,22]. This phasing effect can be large, producing ±20 dB amplitude variations as a function of azimuth depending on the ELF and VLF wave frequency and the distance to the receiver [21,22]. Repeating this experiment with receivers at a variety of azimuthal locations could experimentally determine the importance of the HF phasing effect for cubic ELF and VLF wave generation.

Comparison with theory.—The dual-beam ionospheric HF heating model presented in this work is based on past work [9,22,23], but accounts for electron density changes as a function of HF heating [24]. The model accounts for the HF phasing effect that results from the physical separation of the HF sources [21,22]. Using this model, we aim to produce order-of-magnitude amplitude comparisons with experimental observations, to identify the theoretical altitude of the ELF and VLF source region, and to determine the dominant component of the thermal cubic nonlinearity mechanism that produces the ELF and VLF source. Wave propagation through the *D*-region ionosphere is governed by Maxwell's equations coupled with the 1st- and 2nd-order moments of the Boltzmann equation. Neglecting convection and conduction, the 1st- and 2nd-order moments are given:

$$\frac{\partial \vec{J}}{\partial t} = \frac{q_e^2 N_e}{m_e}\vec{E} + \frac{q_e \mu_0}{m_e}\vec{J} \times \vec{H}_0 - \nu_{\text{eff}}\vec{J}, \tag{1}$$

$$\frac{3}{2}N_e \kappa_B \frac{\partial T_e}{\partial t} = \vec{J}\cdot\vec{E} - \frac{3}{2}\kappa_B T_e \frac{\partial N_e}{\partial t} - L, \tag{2}$$

where $\vec{J}$ is the total current density, $\vec{E}$ is the total wave electric field, $\vec{H}_0$ is the Earth's static magnetic field, q_e is the charge of an electron, m_e is the mass of an electron, N_e is the electron number density, ν_{eff} is the effective electron-neutral collision frequency, T_e is the electron temperature, and L is the electron energy loss rate that depends on N_e, T_e, and T_0, with T_0 being the ambient electron temperature. The above equations assume that the wave magnetic field does not significantly interact with the medium and that the current density $\vec{J}$ is dominated by electron motion. The $\partial N_e/\partial t$ term is determined a four-body model [24,25].

Excitation of the thermal cubic nonlinearity occurs via the $\vec{J}\cdot\vec{E}$ term in Eq. (2). For example, for two high power radio waves at frequencies ω_1 and ω_2, the $\vec{J}\cdot\vec{E}$ term will produce electron temperature oscillations at frequencies $2\omega_1$, $2\omega_2$, $\omega_2 - \omega_1$, $\omega_2 + \omega_1$, and 0. These temperature oscillations in turn produce collision frequency oscillations

at approximately the same frequencies, assuming that the temperature oscillations are small ($< 1\%$). By way of the $\nu_{\text{eff}}\vec{J}$ term in Eq. (1), the collision frequency oscillations produce current density oscillations at frequencies ω_1, $3\omega_1$, ω_2, $3\omega_2$, $\omega_2 + 2\omega_1$, $\omega_2 - 2\omega_1$, $2\omega_2 + \omega_1$, and $2\omega_2 - \omega_1$. We can select the frequencies of the two waves such that the $\omega_2 - 2\omega_1$ component is in the ELF and VLF frequency range, as has been done for the experiment described above.

In this work, the numerical modeling of this process makes use of perturbation theory. The first step is to obtain a good estimate of the average electron temperature and the average electron density under HF heated conditions. For this purpose, Eq. (2) is replaced with the following simplified energy transport equation:

$$\frac{3}{2}N_e\kappa_B\frac{dT_e}{dt} = \sum_m^M \langle \vec{J}_m \cdot \vec{E}_m \rangle - \frac{3}{2}\kappa_B T_e \frac{\partial N_e}{\partial t} - L, \qquad (3)$$

where M represents the total number of HF waves, m identifies the heating wave, and $\langle \cdots \rangle$ represents time averaging. The summation term in Eq. (3) represents the time-averaged power absorbed by the plasma from each of the radio waves, neglecting the nonlinear interactions between the different radio waves.

For the first iteration, Eqs. (1) and (3) are solved together with Maxwell's equations for steady-state heating with two X-mode cw waves, yielding $\vec{E}$, $\vec{J}$, N_{e1}, and T_{e1} as a function of space. The dependence of ν_{eff} and L on T_e and N_e are then linearized about T_{e1} and N_{e1}. We determined by model evaluation that oscillations of these quantities do not significantly depend on N_e, and we have neglected this dependence in our linearization. The previous iteration's values are then substituted into Eqs. (1) and (2) to evaluate the nonlinear components of $\vec{J} \cdot \vec{E}$ and $\nu_{\text{eff}}\vec{J}$. The process may be repeated indefinitely, using the updated values of ν and $\vec{J}$ at each step, but since we are interested in order-of-magnitude calculations, we stop at the second iteration. At no point in this process do we account for the existence of an auroral electrojet current, so that these calculations are independent of the electrojet. We do not enforce the continuity equation for the nonlinear components, and one would expect additional "loop-back currents" to be generated as a result. Based on past work, however, we expect our calculation of the ELF and VLF B field on the ground to be accurate within ~75 km of HAARP [12].

The ambient electron density and electron temperature profiles employed in this work are shown in Fig. 4. These profiles have been used in previous work [9,23]. The ambient electron temperature and neutral density profiles are provided by the MSISE-90 Atmosphere Model [26–28].

For Oasis, the twelve electron density and electron temperature profile combinations produce a propagation delay varying from 0.50 to 0.60 msec and an ELF and VLF magnitude varying from −40 to −15 dB-pT as a function of profile combination. At Paradise, propagation delays vary from 0.65 to 0.75 msec and ELF and VLF magnitudes vary from −50 to −25 dB-pT as a function of profile combination. The propagation delays correspond to ELF and VLF source altitudes between 73 and 91 km altitude, consistent with a D-region source location. The propagation delays and ELF and VLF amplitudes are very reasonable compared to the experimental observations shown in the previous section. Having demonstrated that our theoretical modeling results are reasonably consistent with experimental observations, we now focus on the nonlinear components that are responsible for generating the ELF and VLF source region.

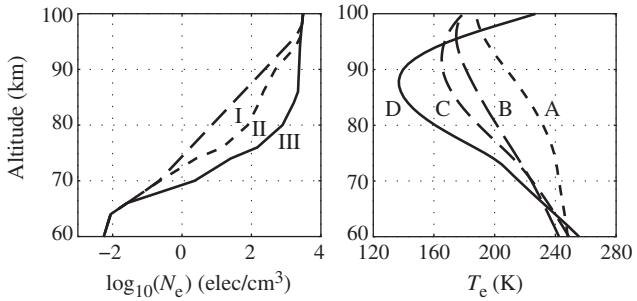

FIG. 4. Electron density (left) and electron temperature (right) profiles used in this work.

For the two-step process utilized in this work, there are three field combinations that generate ELF and VLF waves at frequency $|\omega_2 - 2\omega_1|$. For the first combination, the $\vec{J}_1 \cdot \vec{E}_1$ term produces an electron temperature oscillation at frequency $2\omega_1$, which when mixed with the current density $\vec{J}_2$ produces the ELF and VLF source current density shown in the top panel of Fig. 5. This component produces an annular-shaped ELF and VLF source region of particularly low magnitude. The annular shape results from the fact that the $\vec{J}_1 \cdot \vec{E}_1$ term (at frequency $2\omega_1$) goes to

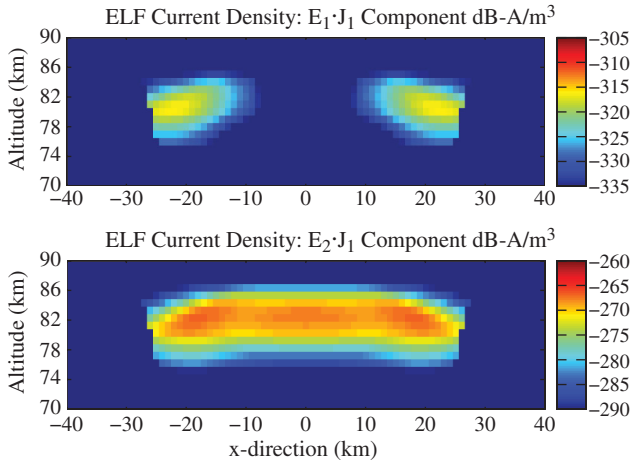

FIG. 5 (color). Modeled ELF and VLF source current densities for ν at frequency $2\omega_1$ (top) and $\omega_2 - \omega_1$ (bottom).

zero for perfectly circularly polarized waves, a result that occurs when the fields propagate parallel to the Earth's magnetic field line. The second and third combinations produce ELF and VLF waves by inducing electron temperature oscillations at frequency $\omega_2 - \omega_1$ that in turn mix with current density $\vec{J}_1$. The spatial distribution for the ELF and VLF source current density associated with $\vec{J}_1 \cdot \vec{E}_2$ mixing is shown in the bottom panel of Fig. 5. The $\vec{J}_1 \cdot \vec{E}_2$ combination produces ~5 dB larger ELF and VLF source magnitudes than the $\vec{J}_2 \cdot \vec{E}_1$ combination (not shown). We note that the top and bottom panels have dramatically different color scales. The ELF and VLF source current densities for the second and third combinations are ~50 dB stronger than those generated by the first combination. While the theoretical results shown in Fig. 5 are for ELF waves at 2 kHz, all of our modeling results produced similar effects as a function of profile combination and ELF and VLF frequency.

Discussion.—ELF and VLF waves generated by excitation of the thermal cubic nonlinearity are observed for the first time at HAARP, and the cubic ELF and VLF source region is experimentally determined to lie within the *D*-region ionosphere. Observations at HAARP are ~5–100 times stronger than at the Sura heating facility [19]. Cubic ELF and VLF wave generation is ~30 dB weaker than auroral electrojet modulation in the 1–5 kHz range [29] and ~10 dB weaker in the 16–20 kHz range [30]. It is also ~3–6 dB weaker than the signals reported to be generated by the ionospheric current drive (ICD) mechanism [15], but cubic generation is strongest at higher frequencies (> 10 kHz), whereas the ICD is reported to be strongest at lower frequencies (< 100 Hz). Cubic wave generation is also highly dependent on the ambient ionospheric conditions, and based on diagnostic observations, higher *D*-region electron densities tend to produce higher cubic ELF and VLF amplitudes.

Numerical simulations provide reasonable estimates of the observed ELF and VLF amplitudes and the observed ELF and VLF propagation delays. For HAARP latitudes, the dominant cubic mechanism producing ELF and VLF radiation consists of collision frequency oscillations at frequency $\omega_2 - \omega_1$ mixing with the polarization current density at frequency ω_1 to produce ELF and VLF waves at frequency $|\omega_2 - 2\omega_1|$. This new understanding of the excitation of the thermal cubic nonlinearity presents an additional avenue for investigating methods of ELF and VLF wave generation that are independent of the strength of the auroral electrojet.

This work is supported by DARPA Contract No. HR0011-09-C-0099, AFRL Grant No. FA9453-12-1-00246, DARPA Grant No. HR0011-10-1-0061 (with subaward UF-EIES-1005017-UCD to CU Denver), NSF Grants No. AGS-0940248 and No. PLR-1246275, and ONR Grant No. N000141010909 to the University of Florida.

*Corresponding author.
moore@ece.ufl.edu

[1] C. G. Getmantsev, N. A. Zuikov, D. S. Kotik, L. F. Mironenko, N. A. Mityakov, V. O. Rapoport, Y. A. Sazonov, V. Y. Trakhtengerts, and V. Y. Eidman, JETP Lett. **20**, 101 (1974).
[2] P. Stubbe, H. Kopka, M. T. Rietveld, and R. L. Dowden, J. Atmos. Terr. Phys. **44**, 1123 (1982).
[3] R. Barr and P. Stubbe, Radio Sci. **19**, 1111 (1984).
[4] M. T. Rietveld, H. Kopka, and P. Stubbe, J. Atmos. Terr. Phys. **48**, 311 (1986).
[5] K. Papadopoulos, T. Wallace, M. McCarrick, G. M. Milikh, and X. Yang, Plasma Phys. Rep. **29**, 561 (2003).
[6] R. C. Moore, U. S. Inan, T. F. Bell, and E. J. Kennedy, J. Geophys. Res. **112**, A05309 (2007).
[7] M. B. Cohen, U. S. Inan, M. Golkowski, and M. J. McCarrick, J. Geophys. Res. **115**, A02302 (2010).
[8] M. Gołkowski, M. B. Cohen, D. L. Carpenter, and U. S. Inan, J. Geophys. Res. **116**, A04208 (2011).
[9] D. Agrawal, and R. C. Moore, J. Geophys. Res. **117**, A12305 (2012).
[10] P. Stubbe, H. Kopka, and R. L. Dowden, J. Geophys. Res. **86**, 9073 (1981).
[11] M. T. Rietveld, H. Kopka, E. Nielsen, P. Stubbe, and R. L. Dowden, J. Geophys. Res. **88**, 2140 (1983).
[12] J. A. Payne, Ph.D. thesis, Stanford University, Stanford, California, 2007.
[13] G. Jin, M. Spasojevic, M. B. Cohen, U. S. Inan, and N. G. Lehtinen, J. Geophys. Res. **116**, A07310 (2011).
[14] K. Papadopoulos, N. A. Gumerov, X. Shao, I. Doxas, and C. L. Chang, Geophys. Res. Lett. **38**, L12103 (2011).
[15] K. Papadopoulos, C.-L. Chang, J. Labenski, and T. Wallace, Geophys. Res. Lett. **38**, L20107 (2011).
[16] V. L. Ginzburg, *The Propagation of Electromagnetic Waves in Plasmas* (Pergamon, New York, 1964), pp. 456–458.
[17] A. V. Gurevich, *Nonlinear Phenomena in the Ionosphere* (Springer-Verlag, New York, 1978), pp. 196–197.
[18] R. Barr, Geophys. Res. Lett. **23**, 2165 (1996).
[19] D. S. Kotik and E. N. Ermakova, J. Atmos. Sol. Terr. Phys. **60**, 1257 (1998).
[20] S. Fujimaru and R. C. Moore, Radio Sci. **46**, RS0M03 (2011).
[21] R. Barr and P. Stubbe, J. Atmos. Sol. Terr. Phys. **59**, 2265 (1997).
[22] M. B. Cohen, R. C. Moore, M. Golkowski, and N. G. Lehtinen, J. Geophys. Res. **117**, A12310 (2012).
[23] R. C. Moore and D. Agrawal, J. Geophys. Res. **116**, A04217 (2011).
[24] J. V. Rodriguez and U. S. Inan, Geophys. Res. Lett. **21**, 93 (1994).
[25] V. S. Glukhov, V. P. Pasko, and U. S. Inan, J. Geophys. Res. **97**, 16 971 (1992).
[26] *Handbook for MAP*, edited by K. Labitzke, J. J. Barnett, and B. Edwards (SCOSTEP Secretariat, University of Illinois, Urbana, Illinois, 1985), Vol. 16.
[27] A. E. Hedin, J. Geophys. Res. **96**, 1159 (1991).
[28] http://ccmc.gsfc.nasa.gov/modelweb/.
[29] M. B. Cohen and M. Gołkowski, J. Geophys. Res. **118**, 6597 (2013).
[30] R. C. Moore, S. Fujimaru, M. Cohen, M. Gołkowski, and M. J. McCarrick, Geophys. Res. Lett. **39**, L18101 (2012).